Turkish Journal of Electrical Engineering & Computer Sciences

http://journals.tubitak.gov.tr/elektrik/

Research Article

Turk J Elec Eng & Comp Sci
(2017) 25: 1599 – 1611

doi:10.3906/elk-1508-61

Comparative study of conventional modulation schemes in terms of conducted and radiated EMI generated by three-phase inverters

Mohamed SALEM[1], **Mahmoud HAMOUDA**[1,2,*], **Jaleleddine BEN HADJ SLAMA**[1]
[1]Research Unit SAGE, ENISo, University of Sousse, Sousse, Tunisia
[2]Canada Research Chair in Electric Energy Conversion and Power Electronics CRC-EECPE, ETS de Montréal, Québec, Canada

Received: 08.08.2015 • **Accepted/Published Online:** 05.06.2016 • **Final Version:** 29.05.2017

Abstract: In this paper, a comparative study is carried out between the carrier (SPWM), third harmonic injection (THIPWM), and space vector (SVPWM) modulation schemes in terms of conducted (common and differential modes) and radiated electromagnetic interference (EMI) generated by three-phase two-level voltage source inverters. For this purpose, an experimental setup of the converter feeding an induction machine is developed with the aim to measure the conducted emission propagated back into the dc source and the radiated field in the vicinity of the power conversion device. Experimental results are given and analyzed in time and frequency domains. The comparative study between the three modulation methods carried out in the frequency domain shows that the SVPWM method has better EMI performance. Moreover, a high frequency model of the converter feeding the induction machine is simulated using SPICE-based simulation software. Good agreement is found between the experimental and simulation results in terms of conducted interferences.

Key words: Voltage source inverters, pulse width modulation (PWM), electromagnetic interference (EMI), conducted emission, high frequency modeling, near field

1. Introduction

Three-phase voltage source inverters (VSI) are versatile power conversion devices that give potential solutions for many industrials applications [1]. Indeed they are widely utilized for adjustable speed drives [2] and they can also operate as an active rectifier [3], shunt active filter [4], uninterruptible power supply (UPS), STATCOM [5], etc. In recent years, they have become a key device in distributed power generation systems (DGS) and renewable energy applications [6]. They are also used to construct the output stage of indirect matrix converters' topologies [7,8]. Note that for low-voltage applications, the two-level inverter remains to date the best suited topology owing to the reduced number of power semiconductors as compared to the multilevel topologies.

The recent developments in power semiconductors technology have led to the appearance of faster switching devices that enable the power converters to operate at higher switching frequencies, leading therefore to better performance in terms of power density and the quality of the output voltages and currents waveforms. However, the high switching speed of power semiconductors is accompanied by a substantial increase in the pulsed voltages slope (dv/dt). Furthermore, the high switching frequency operation increases in turn the variation rate of the common mode voltage. These phenomena give therefore rise to high frequency leakage

*Correspondence: mahmoudhamouda@yahoo.fr

currents flowing through the stray indictors and parasitic capacitors. These currents provide electromagnetic interference (EMI) propagating in the neighboring of the power conversion system. As reported in the recent literature, the level of EMI noise is widely related to power conversion topologies, PCB layout, switching devices technology, and modulation algorithms [9,10].

Basically, EMI is classified into conducted and radiated emissions. The conducted emission is in turn commonly separated into two modes, namely the conducted mode (CM) and differential mode (DM). The CM emitted currents flow from the converter to the ground and back to the converter. The DM emitted currents flow in and out through the power leads. The standard IEC 61800-3 (category 3) issued by the International Electro-technical Commission (IEC) imposes 76 dBμv as the maximum EMI level of conducted emissions in a frequency range [500 kHz, 30 MHz] for low-voltage industrial motor drives with rated current under 100 A. To meet these requirements, EMI filters must therefore be installed at the input and output sides of the inverter to prevent the propagation of the CM and DM emissions outside their source i.e. the inverter. Usually, the output filter mitigates the current overshoots and oscillations due to the large dv/dt occurring across the load terminals as well as the high frequency components of the common mode voltage. As for the input filter, it must provide a low impedance path to the ground so that the leakage currents go back to the inverter, i.e. it prevents its propagation to the dc source.

Apart from the utilization of input/output filters, the EMI emission can be further reduced at the noise source, i.e. the inverter, using modified PWM algorithms. In this framework, a variety of modulation methods have been proposed to reduce the common mode voltage and/or the number of commutations of the power semiconductors. For example, in [11,12] an active zero state PWM (AZSPWM) method is proposed. It uses the same active vectors to produce the zero switching sequence. In [13], various remote state PWM methods (RSPWM) have been developed. Only active vectors that have the same common mode signature (V_1 to V_6) are used to synthesize the target output voltage reference. Another modified PWM technique, namely the near state PWM (NSPWM), was proposed in [14]. This method uses the two adjacent and near-neighbor active vectors to produce the output voltage reference vector. A comparative study between the aforementioned methods has been reported in [15]. In [16], predictive current control (PCC)-based modulation strategies were proposed to mitigate the common-mode voltage and decrease the harmonic distortion of output currents. In [17,18] several others modified SPWM schemes have been also proposed to reduce the common mode voltage. On the other hand, several random PWM techniques were proposed in [19–21]. Their basic concept is to randomize the modulation parameters with the aim to spread the harmonic spectrum around the switching frequency so that the generated noise remains under the EMI limits.

The problem of EMC/EMI was also widely investigated in the case of multilevel conversion topologies. For example, in [22–24], many optimized and robust PWM methods have been developed to reduce the common mode voltage generated by multilevel converters.

Although a variety of modified PWM techniques were reported in the literature, the conventional PWM schemes such as SPWM, THIPWM, and SVPWM remain until now the most adopted algorithms to perform closed-loop control of electrical drives such as vector control of induction machines, and grid connected converters for photovoltaic and wind energy applications. In such complex applications, the time consumption of the modulation algorithm should be reduced as much as possible so that the processor can achieve the computation of the control law within the sampling period. Moreover, these modulation schemes can easily be implemented on standard timers available on conventional low-cost processors.

In [25], a comparative study between the SPWM, THIPWM, and SVPWM modulation schemes has

been performed in terms of conducted interferences. However, the results found in [25] were based only on experimental investigations. This paper proposes a deeper assessment of conventional modulation schemes in terms of conducted interferences where both experimental and simulation results are given and discussed. The comparative study is also based on the radiated field emitted by the power converter.

This paper is therefore organized as follows: section 2 describes the experimental setup built in the laboratory with the aim to perform measurements of the conducted and radiated interferences. In section 3, the experimental results of measurements of conducted and radiated interferences performed with different modulation schemes are given and discussed. In section 4, a high frequency model of the power conversion system is implemented using SPICE-based tools to simulate the conducted interference with the aim to validate the evaluation obtained with the experimental method. Finally, some concluding remarks are given in section 5. Note that details about the theoretical principle of the PWM techniques under study (SPWM, THIPWM, and SVPWM) are given in [9].

2. Experimental setup

2.1. Experimental setup description

A simplified photo of a laboratory prototype of the power conversion system is shown in Figure 1a. Its equivalent electrical schema is depicted in Figure 1b. The power circuit of the inverter is constructed using MOS transistors type (N-channel IRFP450). The gating pulses are provided by the PWM modules of the DSP TMS320F2812. An optical isolation between the controller and power circuit is ensured by the HCPL3120 opto-drivers. The software platform is based on Code Composer Studio software CCSV3.1. All tests are carried out with the same parameters; the output frequency is set to $f_0 = 50$ Hz while the modulation index m is equal to 0.7. The switching frequency and turn-on delay time are set to 2.2 kHz and 2.5 μs, respectively.

2.2. Conducted emission measurement

The precise measurement of high frequency emission in order to quantify their EMI impact is a difficult task that requires very accurate devices. The main problems faced are the environment noise, emplacement of measurement devices, choice of frequency range to be analyzed, etc. For a better quantification of the conducted (in common and differential modes) emission, a line impedance stabilization network (LISN) was built and connected between the converter rear end and the dc supply. The common mode and differential mode emissions are deduced from measured signals across the LISN resistors using a digital scope operating at a sampling frequency of 1 GHz. The time domain results are thereafter analyzed in the frequency domain after FFT calculation.

2.3. Radiated emission measurement

With the aim to achieve accurate and efficient measurements of the radiated emission, an automated system was developed. It consists of an antenna fixed to a simple manipulating arm with two degrees of freedom (X,Y) as shown in the photo in Figure 1c and the illustrative diagram in Figure 1d. The antenna consists of a 1.5 mm radius probe placed above the inverter's power circuit and oriented along the Z-axis. The probe is electrically connected to the scope input through a 50 ohm coaxial cable. In order to achieve an accurate placement of the probe along any point above the inverter, a monitoring program was developed by the authors. This program provides an interface, namely "near-field measurement interface", that enables selection of the measurement region and the distance between two consecutive points. It generates thereafter the appropriate control aiming

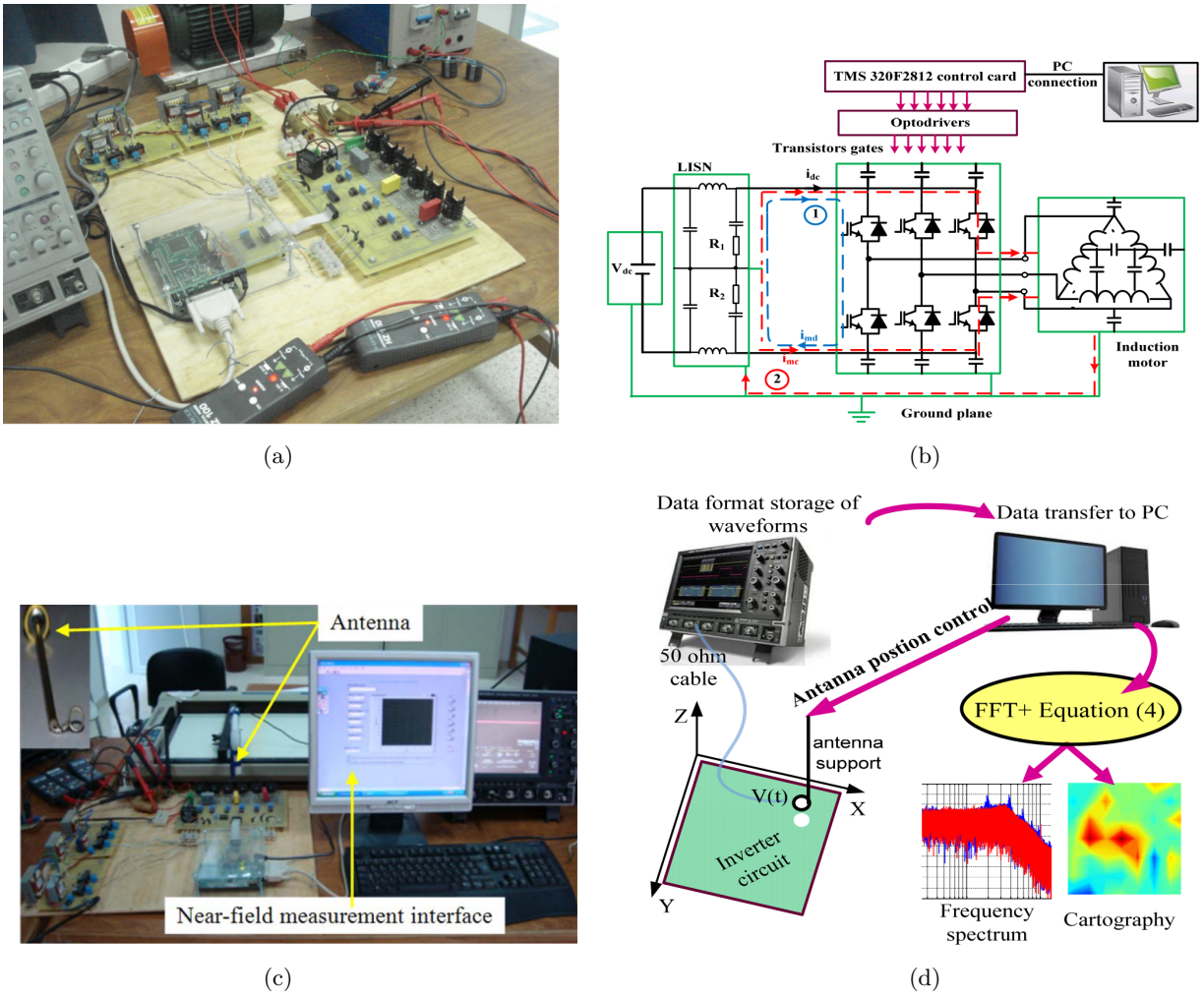

Figure 1. a) Photo of the power conversion system. b) Equivalent electrical schema of the experimental setup including the inverter, control board, LISN, and induction machine: (1) example of differential mode current-loop, (2) example of common mode current-loop. c) Photo of the setup used for the measurement of radiated disturbances. d) Illustrative diagram of the procedure utilized to obtain the frequency spectrum and cartography of the radiated field.

at positioning the antenna in the target position in the (X,Y)-plane. Once the antenna is correctly positioned, the probe voltage is saved in the scope memory as a data format file. After each measurement test, the saved data file is transferred to the PC to be processed by the time to frequency transformation (FFT) to obtain the frequency spectrum of the radiated field using Eq. (4), which is explained in the subsequent paragraph. When all measurements are performed in different points above the inverter, we can also deduce the magnetic field cartography. The latter gives the radiated field amplitude for a specific radiated frequency in each inverter's region.

The relationship between the voltage across the probe and the radiated field above the measurement point can be determined based on Faraday's law. Indeed, the circular conductor loop of the probe placed in a time varying magnetic field induces a voltage $V(t)$ also referred to as electromotive force such that

$$V(t) = \oint \frac{-\partial B}{\partial t} dS \tag{1}$$

Assume the magnetic induction is uniform along the surface S of the probe; the maximum amplitude of the induced voltage V at as specific frequency f of the magnetic field is therefore deduced from (1) such that

$$V(f) = 2\,\pi\,f\,B\,S \tag{2}$$

In (2), B and f are the amplitude and frequency respectively of the magnetic induction. S is the probe surface. Replacing in (2) B by $\mu_0 H$ leads to the following relationship between the amplitude of the radiated field H at the frequency f and the amplitude of the induced voltage at that frequency [26]:

$$H(f) = \frac{V(f)}{2\,\pi\,f\,\mu_0\,S} \tag{3}$$

$\mu_0 = 4\,\pi\ 10^{-7}$ is the vacuum permeability.

The frequency spectrum of the radiated field can therefore be computed by applying the FFT to the temporal signal $V(t)$ and dividing the obtained amplitudes by the constant term $2\,\pi f \mu_0 S$ as reported in (4).

$$H = \frac{FFT\ [V(t)]}{2\,\pi\,f\,\mu_0\,S} \tag{4}$$

3. Experimental results

3.1. Conducted emission

The experimental measurements are carried out with a sampling time of 10 ns. Moreover, no EMI filter is used in the experimental tests. The results are first presented in the time domain to better illustrate the high frequency oscillations phenomenon mainly caused by the switching operation of the power semiconductor devices. The same results are thereafter given in the frequency domain with the aim to perform a comparative study between the frequency spectra obtained with the aforementioned modulation schemes.

In Figures 2a and 2b are displayed the low frequency waveforms of the line-to-line output voltages and load currents obtained with the SVPWM algorithm. Figure 3 shows a zoom of high frequency oscillations in the load current waveform. One can observe high frequency oscillations that obviously occur at the power semiconductors' switching instants. It is also clear that the induced interferences have different amplitudes. In our opinion, this difference is mainly due to equivalent stray inductors seen between each power transistor and the dc power supply that have obviously different values. Figure 4 shows the experimental waveform of one gate pulse (V_{GS}) synchronized with voltages across the LISN resistors V_{R1} and V_{R2}. The same test is also performed by numerical simulation (the simulation setup is described in section 4) where the voltages across the LISN resistors are illustrated in Figure 5. The results confirm that the high frequency transients occur effectively at the same instants of power transistors' commutations. These voltage resonances are caused by the abrupt dv/dt occurring at turn-on/off instants of power semiconductors.

As is well known, time domain analysis is unable to achieve an accurate comparative study between the performances of modulation schemes. Therefore, the above time domain results are transferred into the frequency domain to perform the frequency spectra of generated interferences. In Figures 6 and 7 are given the frequency spectra of common mode and differential mode conducted interferences obtained with the experimental study. In the frequency range varying from 500 kHz to 50 MHz, the SPWM modulation method produces higher amplitude peaks than the SVPWM and THIPWM techniques in both differential and common mode voltages. The most significant amplitude peaks are located at 2 MHz, 3.8 MHz, 5.8 MHz, 10 MHz, 30 MHz, and 48

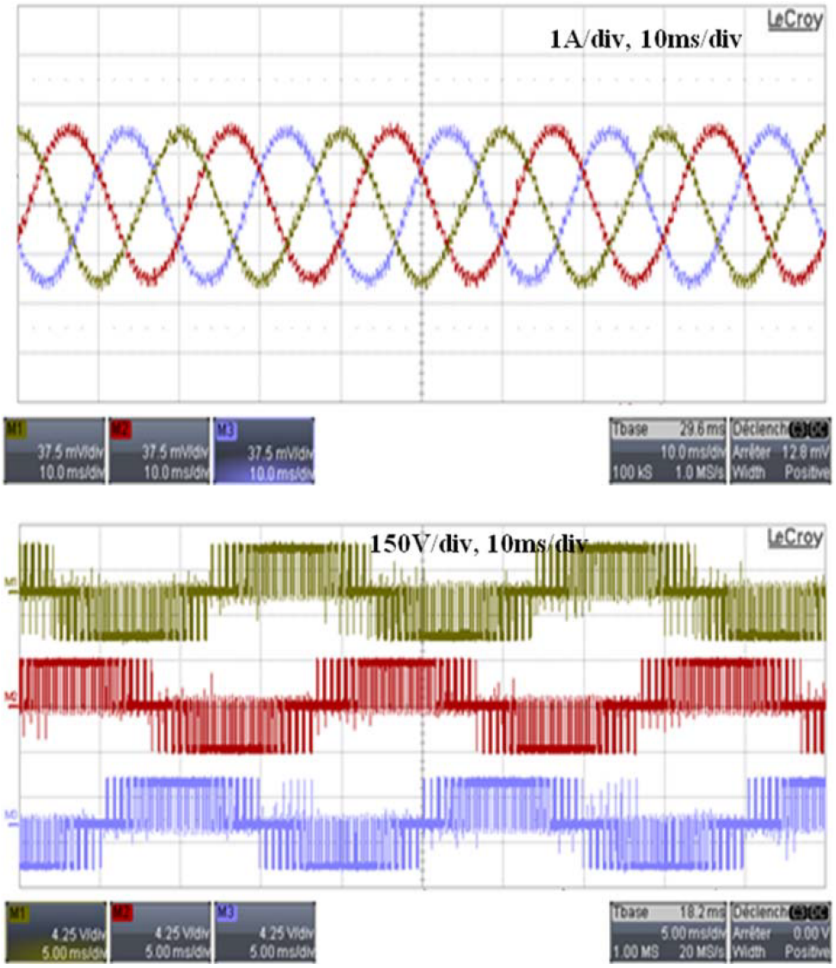

Figure 2. a) Experimental waveforms of load currents waveforms obtained with the SVPWM algorithm. b) Experimental waveforms of the line-to-line output voltages obtained with the SVPWM algorithm.

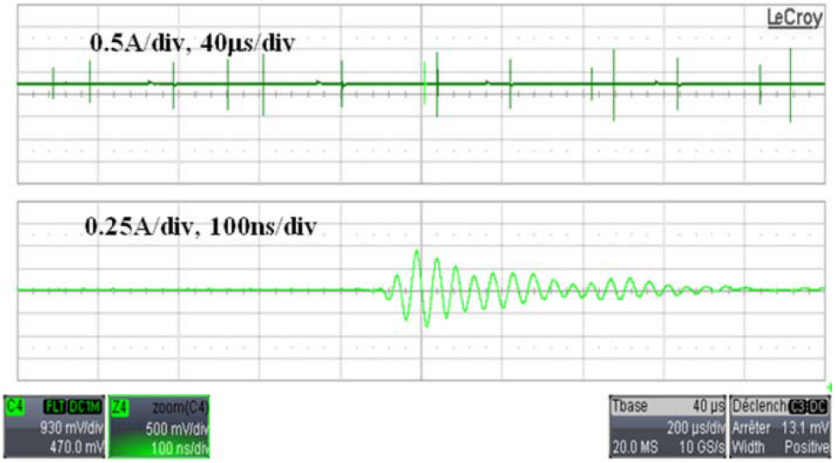

Figure 3. Zoom of the load currents waveforms illustrated in Figure 2a (top) and zoom of one oscillation occurring at a switching instant (bottom).

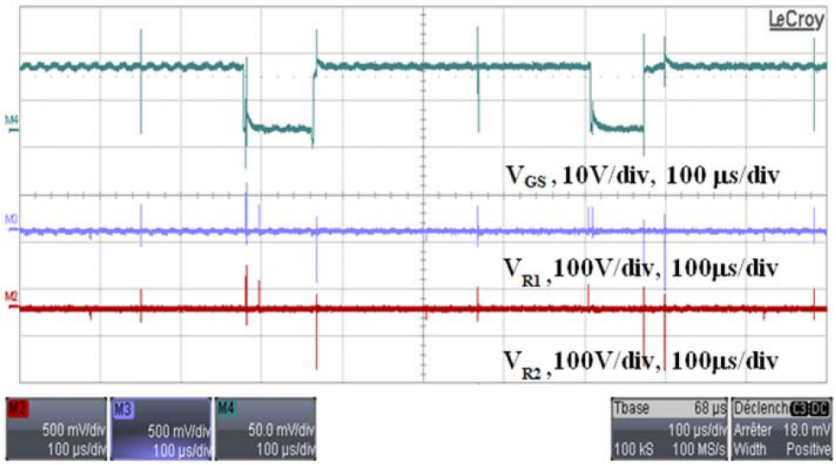

Figure 4. Gate pulse V_{GS} of one transistor (top) synchronized with V_{R1} (middle) and V_{R2} (bottom) measured across the LISN resistors.

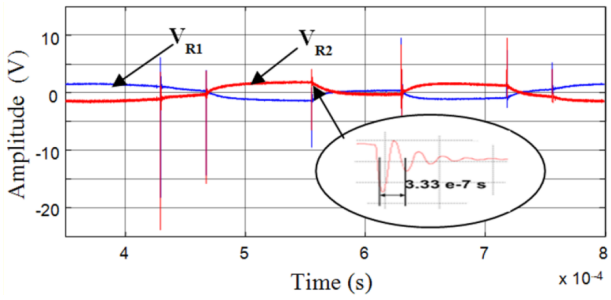

Figure 5. LISN voltage across V_{R1} and V_{R2} obtained with numerical simulations.

MHz. Moreover, it is clear that in this high frequency range the SVPWM generates effectively less conducted interferences than the remaining modulation schemes (SPWM and THIPWM), where the amplitude decrease can reach 6 dBμV. One can also observe that the conducted EMI exceeds the limits prescribed by the standard IEC 61800-3 category 3. In particular, the interference peak at the frequency of 2 MHz exceeds the prescribed limits by 19 dBμV with the SPWM algorithm and by 13 dBμV with the SVPWM method. This result is quite obvious and expected since no EMI filters were utilized during the experimental tests to mitigate the EMI noise

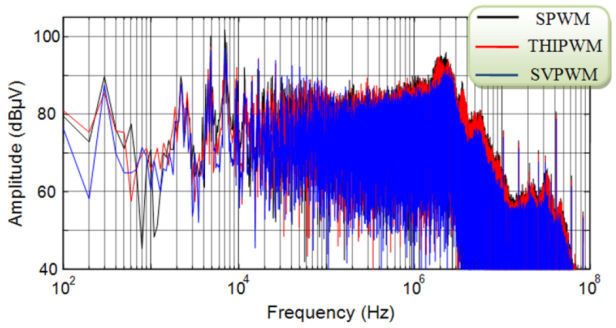

Figure 6. Experimental results of common mode voltage obtained with the three modulation schemes: SVPWM (blue), THIPWM (red), and SPWM (black).

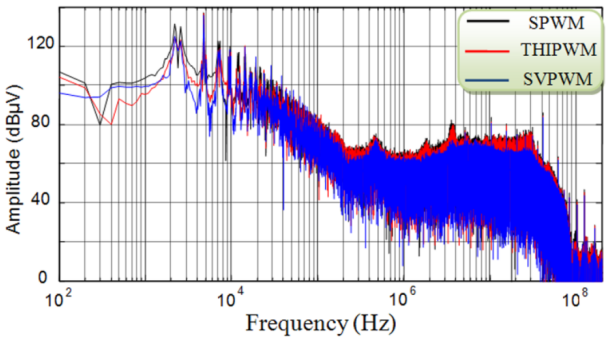

Figure 7. Experimental results of differential mode voltage obtained with the three modulation methods: SVPWM (blue), THIPWM (red), and SPWM (black).

provided by the inverter [27,28]. The obtained conclusions remain valid with and without EMI filters since the attenuation level of the EMI filter remains the same for all PWM methods.

3.2. Radiated emission

In this subsection, a comparative study is carried out in terms of radiated magnetic field generated by the power conversion system. The radiated field measurement method has already been presented in a previous section of this manuscript. Figure 8 displays in the time domain the voltages across the LISN circuit as well as the near field probe voltage that is proportional to the induced field. As can be observed, the radiated signal is mainly caused by the high frequency components of conducted interferences. However, the low-frequency conducted interferences have no significant effects on the radiated field. With the aim to perform an accurate comparison between the three modulation schemes, the frequency spectra of the radiated field have been calculated for two different measurement points over the power circuit using Eq. (4). The obtained results are displayed in Figures 9a and 9b. The comparison between the three radiated fields shows that the obtained results are quite similar to those of conducted interferences. The SPWM technique provides effectively the most intensive radiated field (red curve) whereas the SVPWM method remains the less disturbing technique (blue curve). Indeed, the amplitude of the radiated field is related to the conducted interferences (amplitudes and frequencies) flowing through the emitting structures (equivalent emitting dipoles). The emitting structures are basically closed loops created from a combination of copper paths and power components (transistors, diodes, capacitors, inductors, etc.). Figures 9a and 9b show that the main amplitude peaks are located at 0.5 MHz, 13.8 MHz, and 39.5 MHz. The difference in amplitude between peaks produced by the SPWM (red curve) and SVPWM (blue curve) methods may reach 6 dBμA/m.

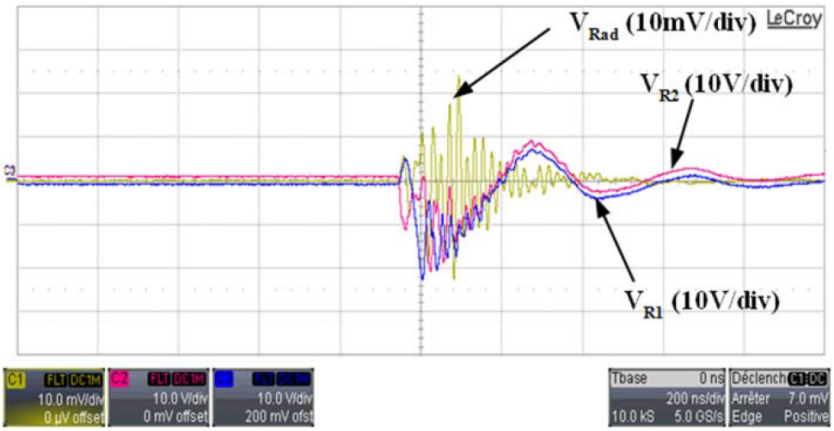

Figure 8. Waveforms of voltages V_{R1} (red) and V_{R2} (blue) across the LISN superposed with the probe voltage V_{Rad} induced by the radiated field (yellow).

In order to emphasize the obtained results, cartographies of the radiated field above the power conversion circuit have been performed at the frequency of 13.8 MHz as illustrated in Figures 10a and 10b. As can be observed, the radiated field amplitude is not uniform over the power circuit surface. This is due to the fact that the resonant currents are going through structures with different surfaces; therefore they have different amplitudes. When analyzing the measured cartographies, we notice more intensive amplitudes of the magnetic field in the superior part. This is due to the presence of the power components in this region. The comparison between the results of Figure 10a (SPWM) and Figure 10b (SVPWM) shows clearly that the surface of the

most disturbing regions in Figure 10a is much more important than that of the regions located in Figure 10b. This result confirms that the SVPWM method effectively generates the lowest radiated field.

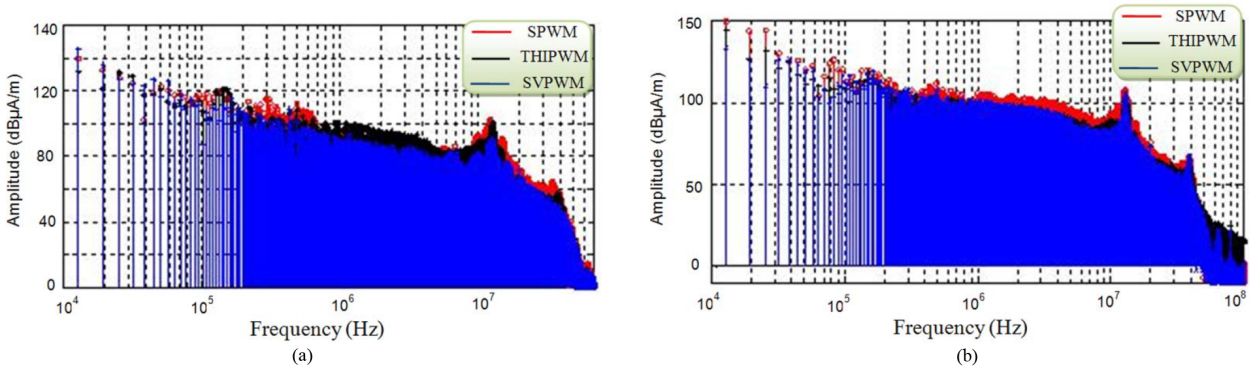

Figure 9. Radiated noise obtained with the three modulations schemes (a) in region 1, (b) in region 2.

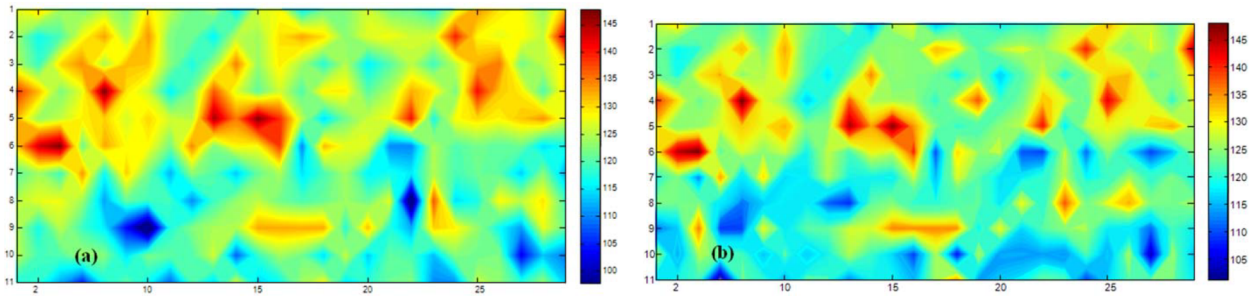

Figure 10. Cartographies of radiated magnetic field (dBμA/m) measured above the power conversion circuit at a frequency of 13.8 MHz: (a) SPWM modulation method, (b) SVPWM method.

4. High frequency modeling and numerical simulations

In order to confirm the conclusions made by experimental investigation, numerical simulations are carried out under the same conditions as the experimental study (sampling time 10 ns, no EMI filter). Note that comparison between simulation and experimental results is beyond the scope of this paper. The high frequency model of the three-phase voltage source inverter used for the simulation is depicted in Figure 11. Each commutation cell is modeled using an advanced Spice model (level three) of the MOSFET. The drain and source are coupled to the ground via 50 pF capacitors. These capacitors emulate the coupling through the heatsink, which constitutes a virtual channel for the propagation of high frequency interferences. Each transistor gate is connected to a programmable voltage supply that emulates the pulses provided at the opto-driver's output side. A parasitic inductor and resistor of the wires between the programmable voltage supply and the gate are also considered ($R_g = 2\ \Omega$ and $L_g = 5$ nH). Each leg includes two parasitic inductors (L_{m1} and L_{12} for leg1) connected in series with the two transistors. Their values are set to 12.5 nH and 5 nH, respectively. The connection between two legs includes two parasitic inductors, namely L_H and L_L. Two capacitors (C_{dc1} and C_{dc2}) are also used to decouple the second and third legs from the stray inductors of the dc-bus bars. Each bus bar is modeled by a parasitic inductor and resistor. Their estimated values are $R_{DB1} = 0.032\ \Omega$, $L_{DB2} = 16.5$ nH for the positive bus-bar and $R_{DB2} = 0.19\ \Omega$, $L_{DB2} = 13.2$ nH for the negative bus-bar. One should point out that the parasitic elements are calculated upon the length and section of their corresponding PCB and wires. On

the other hand, the equivalent circuit model adopted for the induction machine winding is illustrated in Figure 12. The proposed model is quite similar to the one presented in [29].

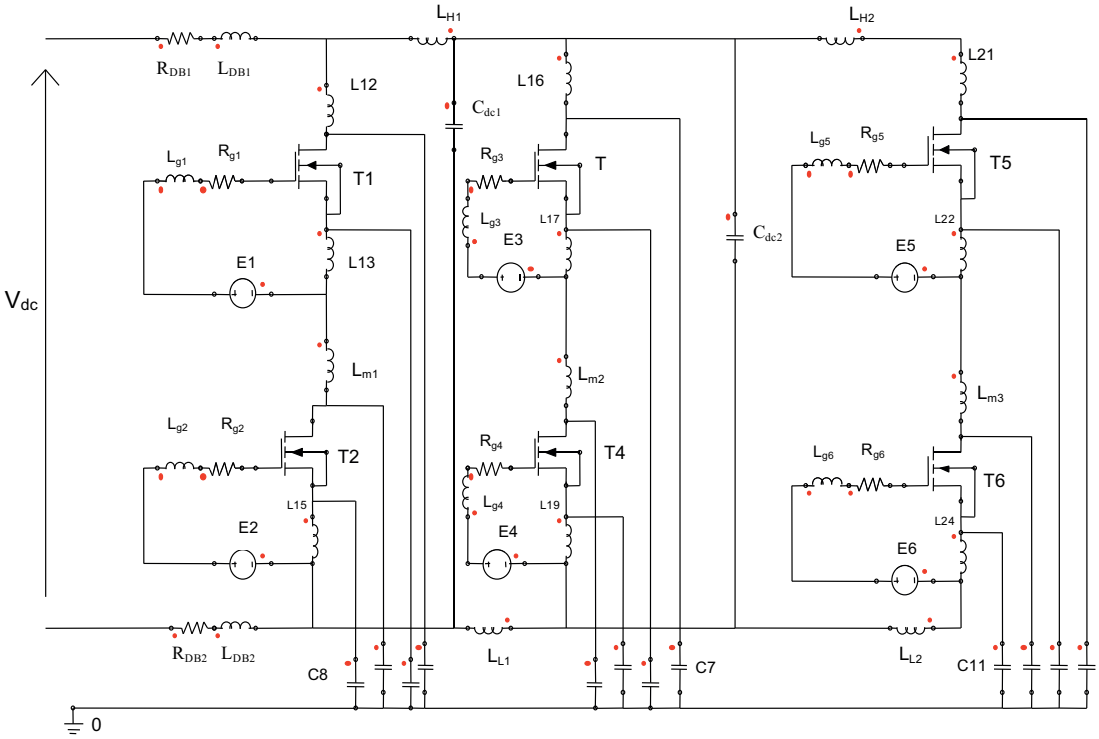

Figure 11. High frequency model of the three-phase voltage source inverter.

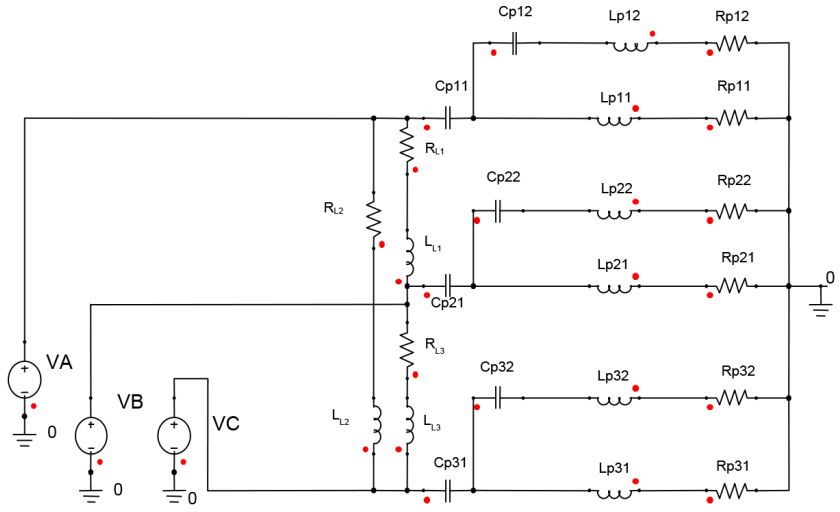

Figure 12. High frequency model of the induction machine, $Cp_{11} = 1$ nF, $Lp_{11} = 20$ μH, $Rp_{11} = 300$ Ω, $Cp_{12} = 240$ pF, $Lp_{12} = 1$ μH, $Rp_{12} = 2$ Ω, $R_{L1} = 17$ Ω, and $L_{L1} = 4$ mH.

To confirm the previous comparative study based on the experimental investigation, simulation results are also transferred into the frequency domain to perform the frequency analysis of the results obtained in the time domain. Figures 13 and 14 show the simulated spectra of conducted interferences including the input common

mode voltages and output common mode currents obtained with the three modulation methods. The results show that in the high frequency range varying from 500 kHz to 30 MHz the most significant peaks obtained with simulation are located at 250 kHz, 450 kHz, 700 kHz, 1 MHz, 1.5 MHz, 2 MHz, and 10 MHz. The analysis of input common mode voltage obtained by numerical simulations illustrated in Figure 13 and experimental results in Figure 6 shows a small difference between the values of resonant frequencies. In our opinion, this difference is due to estimation errors of parasitic elements used in the simulated model. On the other hand, one can clearly observe that the SPWM modulation method produces higher amplitude peaks than the THIPWM and SVPWM techniques in both input common mode voltages and output common mode currents. Moreover, the SVPWM generates less conducted interferences than the remaining two modulation schemes, where the amplitude decrease can reach 5 dBμV. These results emphasize the effectiveness of the experimental evaluation as well as the superiority of the SVPWM algorithm over the SPWM and THIPWM algorithms.

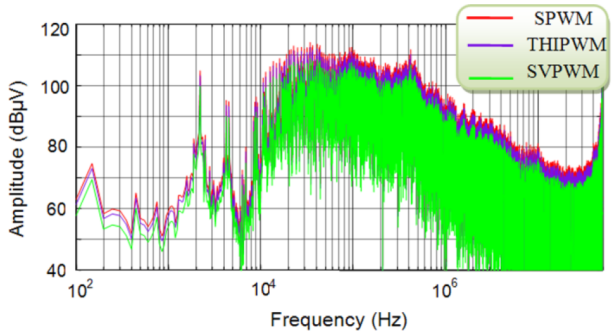

Figure 13. Simulated input common mode voltage obtained with the three modulation methods: SVPWM (green), THIPWM (blue), and SPWM (red).

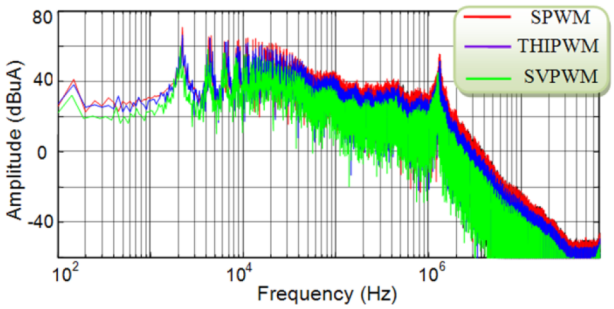

Figure 14. Simulated output common mode current obtained with the three modulation methods: SVPWM (green), THIPWM (blue), and SPWM (red).

5. Conclusion

In this paper a comparative study between three conventional modulation algorithms was carried out in terms of common and differential modes of the conducted interferences as well as in terms of the emitted radiated field. Experimental and simulation results were presented and discussed. The frequency domain analysis showed that the SVPWM modulation technique provides the best performance in terms of conducted and radiated interferences. Meanwhile, the SPWM technique is the most disturbing method. On the other hand, high frequency modeling of the power conversion system has been proposed and implemented using Spice-based software. Good agreement was also found between measured and simulated results related to conducted interferences.

References

[1] Marzouki A, Hamouda M, Fnaiech, F. A review of PWM voltage source converters based industrial applications. In: IEEE 2015 International Conference on Electrical Systems for Aircraft, Railway, Ship Propulsion and Road Vehicles; 3–5 March 2015; Aachen, Germany: IEEE. pp. 1-6.

[2] Moaveni B, Khorshidi M. Robust speed controller design for induction motors based on IFOC and Kharitonov theorem. Turk J Electr Eng & Comp Sci 2015; 23: 1173-1186.

[3] Marzouki A, Hamouda M, Fnaiech F. A hybrid controller for PWM active rectifiers based LCL filters. Compel 2015; 34: 1229-1251.

[4] Kale M, Özdemir E. A new hysteresis band current control technique for a shunt active filter. Turk J Electr Eng & Comp Sci 2015; 23: 654-665.

[5] Sepulveda CA, Munoz JA, Espinoza JR, Figueroa ME, Baier CR. FPGA v/s DSP Performance Comparison for a VSC-Based STATCOM Control Application. IEEE T Ind Inform 2013; 9: 1351-1360.

[6] Lahouar FZ, Hamouda M, Ben Hadj Slama J, Ben Mustapha F. Comparative study between two and three-level topologies of grid-connected photovoltaic converters. In: IEEE 2014 International Renewable Energy Congress; 25–27 March 2014; Hammamet, Tunisia: IEEE. pp. 1-6.

[7] Hamouda M, Blanchette HF, Al-Haddad K. Indirect matrix converters' enhanced commutation method. IEEE T Ind Electron 2015; 62: 671-679.

[8] Hamouda M, Blanchette HF, Al-Haddad K, Fnaiech F. Unity power factor operation of indirect matrix converter tied to unbalanced grid. IEEE T Power Electr 2016; 31: 1095-1107.

[9] Touré B, Schanen JL, Gerbaud L, Avenas Y, Ruelland R, DeMaglie R, Meynard T. EMI study of a 70kW interleaved three-phase inverter. In IEEE 2012 Energy Conversion Congress and Exposition; 5–20 September 2012; Birmingham, UK: IEEE. pp. 623-628.

[10] Ben Hadj Slama J, Hrigua S, Costa F, Revol B, Gautier C. Relevant parameters of SPICE3 MOSFET model for EMC analysis. In: IEEE 2009 International Symposium on Electromagnetic Compatibility; 17–22 August 2009; Austin, USA: IEEE. pp. 319-323.

[11] Tallam RM, Kerkman RJ, Leggate D, Lukaszewski RA. Common-mode voltage reduction PWM algorithm for ac drives. IEEE T Ind Appl 2010; 46: 1959-1969.

[12] Hava AM, Un E. Performance analysis of reduced common-mode voltage PWM methods and comparison with standard PWM methods for three-phase voltage-source inverters. IEEE T Power Electr 2009; 24: 241-252.

[13] Cavalcanti MC, de Oliveria KC, de Farias AM, Neves FAS, Azevedo GMS, Camboim FC. Modulation techniques to eliminate leakage currents in transformerless three-phase photovoltaic systems IEEE T Ind Electron 2010; 7: 1360-1368.

[14] Un E, Hava AM. A near-state PWM method with reduced switching losses and reduced common-mode voltage for three-phase voltage source inverters. IEEE T Ind Appl 2009; 45: 782-793.

[15] Hou CC, Shih CC, Cheng PT, Hava AM. Common-mode voltage reduction pulsewidth modulation techniques for three-phase grid-connected converters. IEEE T Power Electr 2013; 28: 1971-1979.

[16] Hoseini SK, Adabi J, Sheikholeslami A. Predictive modulation schemes to reduce common-mode voltage in three-phase inverters-fed AC drive systems. IET Power Electron 2013; 27: 840-849.

[17] Zawodniok M, Kimball JW. Reducing common-mode voltage in three-phase sine-triangle PWM with interleaved carriers. IEEE T Power Electr 2011; 26: 2229-2236.

[18] Huang J, Xiong R, Wang Z, Zuo W, Zhou Y, Shi H. A novel SPWM control strategy to reduce common-mode voltage in three-phase four-leg inverters. In: IEEE 2008 International Conference on Electrical Machines and Systems; 17–20 October 2008; Wuhan, China: IEEE. pp. 1526-1530.

[19] El Khamlichi Drissi K, Luk PCK, Wang B. Effects of symmetric distribution laws on spectral power density in randomized PWM. IEEE Power Electron Lett 2003; 1: 41-44.

[20] Kaboli S. Application of random PWM technique for reducing the conducted electromagnetic emissions in active filters. IEEE T Ind Electron 2007; 54. 2333-2343.

[21] Khan H, Miliani El-H, El Khamlichi Drissi K. Discontinuous random space vector modulation for electric drives: a digital approach. IEEE T Power Electr 2012; 27: 4944-4951.

[22] Chaturvedi PK, Jain S, Agrawal P. Harmonics and common mode voltage reduction in multilevel SPWM technique. In: IEEE 2008 Annual India Conference; 11–13 December. 2008; Kanpur, India: IEEE. pp. 447-452.

[23] Renge M, Suryawanshi HM, Borghate VB, Ramteke MR. Multilevel inverter to eliminate common mode voltage in induction motor drives. In: IEEE 2006 International Conference on Industrial Technology; 15–17 December 2006; Mumbai, India: IEEE. pp. 2354-2358.

[24] Saribulut L, Tümay M. Robust space vector modulation technique for unbalance voltage disturbances. Electric Power Syst Res 2010; 80: 1364-1374.

[25] Salem M, Hamouda M, Ben Hadj Slama J. Performance assessment of conventional modulation schemes in terms of conducted EMI generated by PWM inverters. In: IEEE 2014 International Conference on Green Energy; 25–27 March 2014; Sfax, Tunisia: IEEE. pp. 207-212.

[26] Saidi S, Ben Hadj Slama J. Near-field technique based on PZMI, GA and ANN: application to power electronics systems. IEEE T Electromagn C 2014; 56: 784-791.

[27] Akagi H, Shimizu T. Attenuation of conducted EMI emissions from an inverter-driven motor. IEEE T Power Electr 2008; 23: 282-290.

[28] Gong X. Conducted EMI in inverters with SiC transistors. PhD, Dalian University of Technology, Dalian, China, 2013.

[29] Labrousse B, Revol B, Costa F. Fast reconstitution method (FRM) to compute the broadband spectrum of common mode conducted disturbances. IEEE T Electromagn C 2013; 55: 284-256.